THESIS FOR THE DEGREE OF LICENCIATE OF ENGINEERING

Fabrication, development and characterization of a waveguide microscopy device for biological applications

Mokhtar Mapar

Department of Physics

CHALMERS UNIVERSITY OF TECHNOLOGY

Göteborg, Sweden 2016

Fabrication, development and characterization of a waveguide device for biological applications

Mokhtar Mapar

Department of Physics
Chalmers University of Technology
SE-412 96 Göteborg
Sweden
Telephone + 46 (0)31-772 1000

Cover picture: Bilayer formation observed using waveguide based scattering microscopy.

Printed at Chalmers Reproservice
Göteborg, Sweden 2016

Fabrication, development and characterization of a waveguide device for biological applications

Mokhtar Mapar
Department of Physics
Chalmers University of Technology

Abstract

Our understanding of biological systems has advanced significantly thanks to the development of microscopy methods and suitable biological assays. Surface based methods have increasingly gained interest thanks to their superior sensitivity and ease of use. Still, most of them, such as quartz crystal microbalance (QCM) and surface plasmon resonance (SPR), provide information based on ensemble averaging of biomolecular interactions. In contrast, surface-sensitive microscopy methods provide the possibility to study biological processes on an individual biomolecular basis.

Total internal reflection fluorescent (TIRF) microscopy is a surface-sensitive microscopy method that reaches sensitivities down to the level of single molecules, but it is limited by the need to fluorescently label the interaction partners. On the contrary, waveguide-based evanescent-light scattering microscopy provides a label-free surface-sensitive imaging technique that can also benefit from fluorescent labeling if desired.

Here we present ongoing efforts to further develop a waveguide-based platform for evanescent light-scattering microscopy. By adopting the fabrication and processing steps to a transparent substrate and adding compatible microfluidics, we can now use high NA oil-immersion objectives thereby collecting more light and resolve details that could not be resolved when fabricated on an opaque substrate. Further, well-controlled microfluidic handling makes it possible to perform more complicated experiments and extract data on interaction dynamics. Moreover an image processing code has been developed that can be applied to the different experimental sequences, including both waveguide fluorescent and scattering modes, and thereby extract otherwise hidden information in the experimental data.

Keywords: Waveguide scattering microscopy, Waveguide fluorescent microscopy, Image processing, Nanofabrication, Virus, Lipid bilayer

Appended publications

Paper I

Low temperature fabrication of a symmetric hybrid organic-inorganic planar waveguide platform for evanescent wave microscopy in aqueous environments

Björn Agnarsson, Mokhtar Mapar, Fredrik Höök*

In Manuscript

Contribution: I was involved in performing the experiment regarding benchmarking the waveguide. I did the image processing and participated in the analysis of the results.

Paper II

Evanescent Light-Scattering Microscopy for Label-Free Interfacial Imaging: From Single Sub-100nm Vesicles to Live Cells

B. Agnarsson, A. Lundgren, A. Gunnarsson, M. Rabe, A. Kunze, M. Mapar, L.Simonsson, M. Bally, V. P. Zhdanov and F. Hook

ACS Nano 9(12): 11849-11862.2

Contribution: I was involved in some of the experiments, the image processing and the data analysis.

Paper III

Fabrication and Characterization of a transparent waveguide device with controlled liquid exchange

Mokhtar Mapar, Björn Agnarsson, Fredrik Höök*

In Manuscript

Contribution: I did all the fabrication development, experiments, image processing and data analysis. I also contributed to the writing of the draft.

Table of Contents

Abbreviations

WGF	Waveguide Fluorescent
WGS	Waveguide Scattering
TIRF	Total internal reflection fluorescent microscopy
RIE	Reactive ion etching
DRIE	Deep reactive ion etching
NA	Numerical aperture
SBR	Signal to background ratio
SNR	Signal to noise ratio
LSPR	Local Surface Plasmon Resonance

1 Introduction

Nanotechnology emerged from microelectronic processing techniques and has spread into almost all fields of science[1–4]. In fact, by contributing entirely new possibilities, nanotechnology has become one of the forces that brings complementary scientific and research directions closer together. It has already contributed to development of many new sensor technologies[5–9] and improved efficiency[10] and yield with respect to energy consumption, storage capacity etc[11]. Life science is one of the disciplines that has benefited significantly from advances in nanotechnology, manifested in the development of for example nanoplasmonics sensors[12–14], microfluidics[4,15], lab on a chip methods[16,17], to mention a few.

One of the bridges that nanotechnology has contributed is that between optics and biology. Optics has a long history and an important place in biological science. Soon after the invention of the first optical microscope in 1595[18], it was used in studies of biological tissues and has since then been a corner stone for many biological discoveries. Accordingly, a multitude of different configurations of optical microscopes have been developed to specifically address the needs in bioscience, the most recent one being super resolution microscopy which in 2014 was awarded the Nobel prize in Chemistry[19–21].

Total internal reflection fluorescent (TIRF) microscopy is another important microscopy method, developed for biological applications in the 1980s[22]. It has been extensively used to study single molecules[23] and various cellular phenomena[24,25] and to investigate interaction forces[26] and for obtaining sub-wavelength resolution[27]. TIRF microscopy employs high NA objectives to shine light at an angle larger than the critical angle for light passage across a glass-water (in case of aqueous measurement) interface. The total internal reflection of the light at the interface induces a non-radiative evanescent field on the sample side that propagates along the surface and decays as it goes deeper in the sample. The result is a thin sheet of light illuminating only the very close vicinity of the interface. The penetration depth depends on the wavelength, illumination angle and the refractive indexes of the environment and the substrate.

During or after immobilization of the entity of interest, one can continuously monitor changes in the fluorescence properties which has enabled the use of TIRF in for example single particle studies[28–30]. Nevertheless, standard TIRF microscopes are constrained by the availability of high NA oil immersion objectives, inverted microscopes, and the compatibility of the subject of interest with available fluorescent dies. For a specific excitation wavelength and sample environment, the penetration depth can only be adjusted within 0.3-0.8 times the wavelength by varying the angle of incident. Furthermore, multi-wavelength excitation can be difficult to achieve from a practical perspective. These limitations leave some room for competing techniques.

An alternative surface-sensitive microscopy method that has become available thanks to advancement in nanotechnology fabrication techniques is waveguide based evanescent microscopy[31]. This method exploits the evanescent light, traveling along the cladding of a waveguide, to generate a similar interface-confined sheet of light as that of TIRF microscopy[32–35]. In contrast to TIRF microscopy, where the light exciting the evanescent modes is reflected back to the objective, the exciting light is in waveguide-based microcopy confined to the core of the waveguide. This makes it possible to perform evanescent light microscopy in scattering mode[36],something that is difficult to achieve using standard TIRF setups. Since surface-based scattering microscopy does not require fluorescent labels, it thus offers an important complement to conventional TIRF. Moreover, by changing the parameters of the fabrication process, such as the material and thickness of the core, one can modify the decay length of the evanescent field in a much wider range than in TIRF[31]. In

addition, waveguide-based imaging can in principle be performed with both upright and inverted microscopy setups with a wide variety of objectives, which makes it more attractive from the user's perspective.

This thesis work has contributed to the development of a waveguide evanescent microscopy setup (Papers I and II). This original device is a planar waveguide with a silicon oxide layer as core and a water refractive index-matching polymer as the cladding, fabricated on a silicon substrate. An opening is made in the top cladding to give access to the evanescent field traveling above the cladding for microscopy measurements. The device is well suited for water immersion-objective-equipped upright microscopes, with the sample handling being done by manual pipetting during liquid exchange.

The main focus of the thesis work, though, has been the further development of this waveguide device to make it compatible with inverted microscopes and other varieties of objectives and better liquid handling. By adopting the fabrication process to glass substrates, one can use both air and oil immersion objectives in an inverted configuration. Further, with an inverted microscope the rays of light constructing the image do not pass through the solution and will not be scattered or distorted by the content of the sample. Due to higher refractive index of glass than that of water, more light is coupled in the glass than water in the near field and therefore one may expect to collect a brighter image. Using oil immersion objective, one can also extend the accessible numerical aperture from 1.1 of water immersion to as high as 1.49. As presented in Paper III, this has a huge impact on the amount of collected light and thus in principle the details that can be resolved, but was also observed to influence the pattern of the scattered light. Successful implementation of microfluidics was shown to offer better control of liquid exchange, although not yet used to probe interaction kinetics.

2 Theoretical background

Thanks to the development of Information Technology, waveguide-based devices and sensors has been developed for primarily optical communication purposes. Depending on the particular application, these devices can come in different forms and configurations. The most common optical waveguide is an optical fiber, which has a circular cross section. In bioanalytical sensor applications, optical fibers are for example used for local illumination of sensor arrays[37]. When applied for microscopy applications, planar slab waveguides are preferred, since a large planar area becomes illuminated. A slab waveguide has a rectangular cross section, with finite dimension in one direction and (physically) infinite dimension in the other direction, which simplifies the theoretical description. In this chapter the physics of wave propagation in such a waveguide will be discussed.

2.1 Propagation

Light, as all other forms of electromagnetic radiations, can be described by two vector fields; electric field and magnetic field. The electric (**E**) and magnetic (**B**) fields are entangled fields and the relation between them is governed by the Maxwell equations:

$$\nabla \cdot \boldsymbol{D} = \rho \tag{2-1}$$

$$\nabla \cdot \boldsymbol{B} = 0 \tag{2-2}$$

$$\nabla \times \boldsymbol{E} = -\frac{\partial \boldsymbol{B}}{\partial t} \tag{2-3}$$

$$\nabla \times \boldsymbol{H} = \boldsymbol{J} + \frac{\partial \boldsymbol{D}}{\partial t} \tag{2-4}$$

Where ρ is the free charge density, $\mathbf{J}$ is electric current density. The electrical current density is related to the electrical field through the conductivity (σ) of the medium,

$$\boldsymbol{J} = \sigma \boldsymbol{E}. \tag{2-5}$$

D and **H** are electric and magnetic displacement fields which are defined by:

$$\boldsymbol{D} = \varepsilon \boldsymbol{E} \tag{2-6}$$

$$\mathbf{H} = \frac{\boldsymbol{B}}{\mu} \tag{2-7}$$

where ε and μ are the permittivity and permeability of the medium which are related to those properties in vacuum by:

$$\varepsilon = \varepsilon_0 \, \varepsilon_r \tag{2-8}$$

$$\mu = \mu_0 \, \mu_r. \tag{2-9}$$

ε_r and μ_r are called the relative permittivity and permeability of the medium.

For dielectrics and isolators, the absence of free charge entities in the material ($\rho = 0$) results in negligible conductivity, which in turn removes the electric current density from equation 2-4. For these materials the Eigen equation for wave propagation can be derived from Maxwell equations. Applying the curl ($\nabla \times$) operator to equation 2-3 results in,

$$\nabla \times \nabla \times \boldsymbol{E} = -\nabla \times \frac{\partial \boldsymbol{B}}{\partial t} \tag{2-10}$$

Using vector identity $\nabla \times \nabla \times \boldsymbol{E} = \nabla(\nabla \cdot \boldsymbol{E}) - (\nabla \cdot \nabla)\boldsymbol{E}$ and equation 2-1 on the left side and equation 2-4 on the right of the equation leads to Helmholtz equation.

$$\nabla^2 \boldsymbol{E} = \varepsilon \mu \frac{\partial^2 \boldsymbol{E}}{\partial t^2} \tag{2-11}$$

$$\nabla^2 \boldsymbol{E} - \frac{\varepsilon_r \mu_r}{c^2} \frac{\partial^2 \boldsymbol{E}}{\partial t^2} = 0 \tag{2-12}$$

Assuming a time harmonic monochromatic wave, where $\boldsymbol{E}(r,t) = \boldsymbol{E}(r)E(t)$ and $E(t) = e^{-i\omega t}$ one can further simplify the equation to

$$\nabla^2 \boldsymbol{E} + \varepsilon_r \mu_r \frac{\omega^2}{c^2} \boldsymbol{E} = \mathbf{0}. \tag{2-13}$$

The solution to this equation can be expressed in the form of a propagating plane wave:

$$\mathbf{E}(\mathbf{r}, \mathrm{t}) = \mathbf{E}_0 e^{\pm i\boldsymbol{k}\cdot\boldsymbol{r} - \mathrm{i}\omega t} \tag{2-14}$$

where $\boldsymbol{k}$ is the wave vector. The direction of the wave vector defines the direction of propagation and its magnitude, known as wavenumber, represents the spatial frequency of the wave, specifying how fast the wave front evolves in space along the wave vector. The wavenumber is defined by:

$$\boldsymbol{k} = \sqrt{\boldsymbol{\varepsilon_r \mu_r}} \frac{\boldsymbol{\omega}}{\boldsymbol{c}} \tag{2-15}$$

For most optical medium the relative permeability, μ_r, is close to unity and thus the wave number can be simplified to

$$k = n\, k_0 \tag{2-16}$$

where $n = \sqrt{\varepsilon_r}$ is the refractive index of the medium along the polarization vector, and $k_0 = \frac{\omega}{c}$ is the wavenumber in vacuum.

Similarly one can derive a similar formula for magnetic field displacement, H,

$$\nabla^2 \boldsymbol{H} = \varepsilon\mu \frac{\partial^2 \boldsymbol{H}}{\partial t^2} \tag{2-17}$$

$$\nabla^2 \boldsymbol{H} + \varepsilon_r \mu_r \frac{\omega^2}{c^2} \boldsymbol{H} = \mathbf{0} \tag{2-18}$$

$$\mathbf{H}(\mathbf{r}, \mathrm{t}) = \mathbf{H}_0\, e^{-i(\boldsymbol{k}\cdot\boldsymbol{r} - \omega t)} \tag{2-19}$$

2.2 Planar waveguide

A planar dielectric waveguide is a two dimensional guiding system that consists of three layers of material stacked on top of each other (Figure 1). The middle layer that is called core has a higher refractive index at the operating optical wavelength than the cladding layers surrounding it. If the cladding layers have the same refractive index ($n_2 = n_3$), the planar wave guide is called symmetric, otherwise, if not, asymmetric.

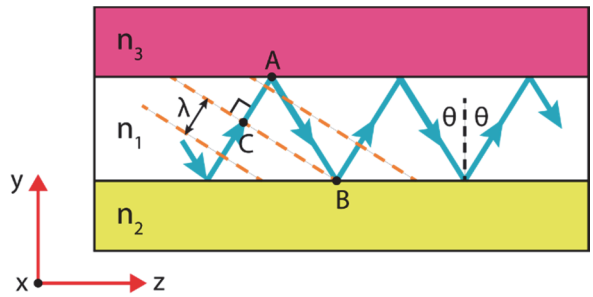

Figure 1. Side wide view of an asymmetric slab waveguide with a ray of light propagating through it. The oblique dashed lines represent the wave front around point C.

The propagation of light inside a waveguide is commonly described either with the help of Maxwell's equations or using geometrical ray optics. Here we start with describing the light behavior in the slab waveguide using ray optics. It helps the reader to develop an intuitive understanding of how the light propagates in the waveguide and how different modes are formed. However, to provide a better understanding of light propagates through the waveguide the picture is complemented with the electromagnetic approach.

1.1.1 Ray Optics approach

Assume a beam of light in form of plane wave being focused to the core on the end-facet of a slab waveguide. If the angle of incident to the core-cladding interface is large enough, the light will undergo a total internal reflection and can potentially propagate through the waveguide in a zigzag fashion (Figure 1). In reality the excitation illumination is typically much wider than core, and therefore one can consider a plane-wave ray of light propagating through the waveguide. The ray is reflected at point A from the upper cladding and consequently at point B at the lower cladding. Although the angle of reflection is unchanged upon total internal reflection, a phase shift, $\varphi(\theta)$, is induced in the reflected light as the reflection coefficient turns into a complex value that depends on the angel of reflection, polarization of light and the refractive index of cladding and core. The constant phase plane of the reflected ray at B now overlaps with that of the first ray at point C. As these two rays share their phase planes if out of phase, they will interfere destructively and the wave will decay as it propagates forward. Therefore, for successful guiding, the parallel rays of light from consecutive reflections must be in phase. Mathematically this can be expressed as:

$$k_1(CA + AB) + 2\varphi(\theta) = 2m\pi \quad (2\text{-}20)$$

Where $k_1 = k_0 n_1 = \frac{2\pi n_1}{\lambda}$ is the wavenuber of the light propagating through the core, and *m* has an integer value. The length of the CA and AB paths can be expressed by

$$CA = \cos(2\theta)\, AB\,, AB = \frac{d}{\cos(\theta)} \quad (2\text{-}21)$$

$$CA + AB = (\cos(2\theta) + 1)\frac{d}{\cos(\theta)} = (2\cos^2(\theta))\frac{d}{\cos(\theta)} = 2d\,\cos(\theta) \quad (2\text{-}22)$$

Plugging this into eq. 1-20 results in:

$$k_1(2d\,\cos(\theta)) + 2\varphi(\theta) = 2m\pi \quad (2\text{-}23)$$

Equation 1-23 places a constrain on the incident angle of the guided rays. For each m there will be one allowed incident angle of θ_m corresponding to a unique propagation mode and its corresponding $\varphi(\theta_m)$ or φ_m for which the light can propagate through the waveguide as long as $\theta_m > \theta_c$ where θ_c is the critical angle for total internal reflection. Each θ_m corresponds to a single *propagation mode* θ_m, and θ_0, corresponding to the largest angle of incident, is generally referred to as the ground or fundamental mode of the waveguide. The phase shift φ_m can be understood as the penetration of the zig-zag ray (for a certain depth δ) into the cladding layers before being reflected.

The propagation constant along the waveguide for each mode can be resolved by projecting the wavevector along the guiding direction,

$$\beta_m = k_1 sin(\theta_m) = k_0 n_{eff}. \quad (2\text{-}24)$$

Considering the total internal reflection condition, $\theta_c < \theta_m < 90$, one can identify the β_m limits compared to the wavenumber in core and cladding,

$$k_0 n_1 sin(\theta_c) < k_0 n_1 sin(\theta_m) < k_0 n_1 sin(90) \quad (2\text{-}25)$$

$$k_0 n_2 < \beta_m < k_0 n_1 \quad (2\text{-}26)$$

$\varphi(\theta_m)$ can further be calculated using appropriate boundary conditions[38,39], and hence, for a given *m* and a set of parameters n_1, n_2, and *d*, a discrete set of reflection angles θ_m can be obtained using equation 2-23 , each corresponding to a unique mode.

1.1.2 Electromagnetics approach

Now we complement the ray optics with an electromagnetic analysis to give the reader a better view of light propagation in a planar waveguide.

The light that travels in the waveguide in TE mode, having its electric field vector perpendicular to the plan of propagation, is still governed by Maxwell's equations, and thus equation 2-13 holds. The light travels along the waveguide in z direction with a wavenumber of β_m, and one can separate the z dependence of the light in the form of a complex exponential coefficient. As the waveguide is semi-infinite in the x direction, the solution to the electric field is not a function of x. Therefore,

$$\boldsymbol{E_x} = \boldsymbol{E_x}(y,z) = \boldsymbol{E_x}(y)e^{i\beta_m z} \tag{2-27}$$

By substituting 2-27 in equation 2-13 we have

$$\nabla_y^2 \boldsymbol{E_x} - \beta_m^2 \, \boldsymbol{E_x} + k^2 \, \boldsymbol{E_x} = \boldsymbol{0} \tag{2-28}$$

$$\frac{\partial^2}{\partial y^2}\boldsymbol{E_x} + (k^2 - \beta_m^2)\boldsymbol{E_x} = \boldsymbol{0} \tag{2-29}$$

where k is the wavenumber for free propagation of light in the medium, which depends on the refractive index. This in turn means that the $(k^2 - \beta_m^2)$ coefficient adopts different values for the core and the cladding. The latter expression is positive for the core and negative for the cladding in the guiding mode according to equation 2-26, and results in an evanescent field in the cladding and a sinusoidal wave profile in the core along the y axis. The wave equations in the upper cladding, core and lower cladding will be as followed

$$\boldsymbol{E_x} = \mathrm{A}\, \mathrm{e}^{-\sqrt{(\beta_m^2 - k_{clad}^2)}\,\mathrm{y}} \mathrm{e}^{i\beta_m z} \tag{2-30}$$

$$\boldsymbol{E_x} = (\mathrm{B}\cos(\sqrt{(k_{core}^2 - \beta_m^2)}\, y) + \mathrm{C}\sin(\sqrt{(k_{core}^2 - \beta_m^2)}\, y)\,)\mathrm{e}^{i\beta_m z} \tag{2-31}$$

$$\boldsymbol{E_x} = \mathrm{D}\, \mathrm{e}^{\sqrt{(\beta_m^2 - k_{clad}^2)}\,\mathrm{y}} \mathrm{e}^{i\beta_m z} \tag{2-32}$$

At higher modes, as β_m^2 decrease due to smaller angle of incident, the $(k_{core}^2 - \beta_m^2)$ and $\left(\beta_m^2 - k_{clad}^2\right)$ respectively increase and decrease, respectively. This results in smaller decay length in the cladding and more oscillations in the core. According to Equations 2-30 and 2-32, the electromagnetic wave created in the cladding, propagates in the *z* direction with an intensity that decays with distance from the core layer. This decaying

behavior can be characterized by a decay length, *d*, represented by the distance at which the intensity of the electric field has dropped to $1/e$ of the value at the interface,

$$\boldsymbol{d} = \frac{\mathbf{1}}{\sqrt{(\beta_m^2 - k_{clad}^2)}} = \frac{\lambda}{2\pi} \frac{\mathbf{1}}{\sqrt{\boldsymbol{n_{eff}^2 - n_{cladding}^2}}} \tag{2-33}$$

This will produce a sheet of light in close vicinity of the core layer in the cladding only.

3 Fabrication and processing

Water constitutes most of the mass of living creatures and most, if not all chemical reaction and transport processes in our body take place in aqueous environment. As a result, for biological studies to be relevant, they must be performed in aqueous media. Further, in microscopy, there is often a need for transparent materials, and many protocols have accordingly been adopted to interface biological entities to glass substrates. Therefore, silicon oxide, which is the main constituent of glass, was chosen as the dielectric core layer of the waveguide chip. To generate a symmetric wave propagation, a highly transparent fluoropolymer called Cytop with a refractive index close to water was used for the cladding. The choice of Cytop as a chemically inert hydrophobic material has been a key defining factor for the majority of the steps in the fabrication process. This chapter expands on these steps and what measures that have been taken to achieve a reliable and reproducible fabrication process. Later in the chapter we describe how to combine the waveguide with microfluidics to improve the liquid handling in the experiments.

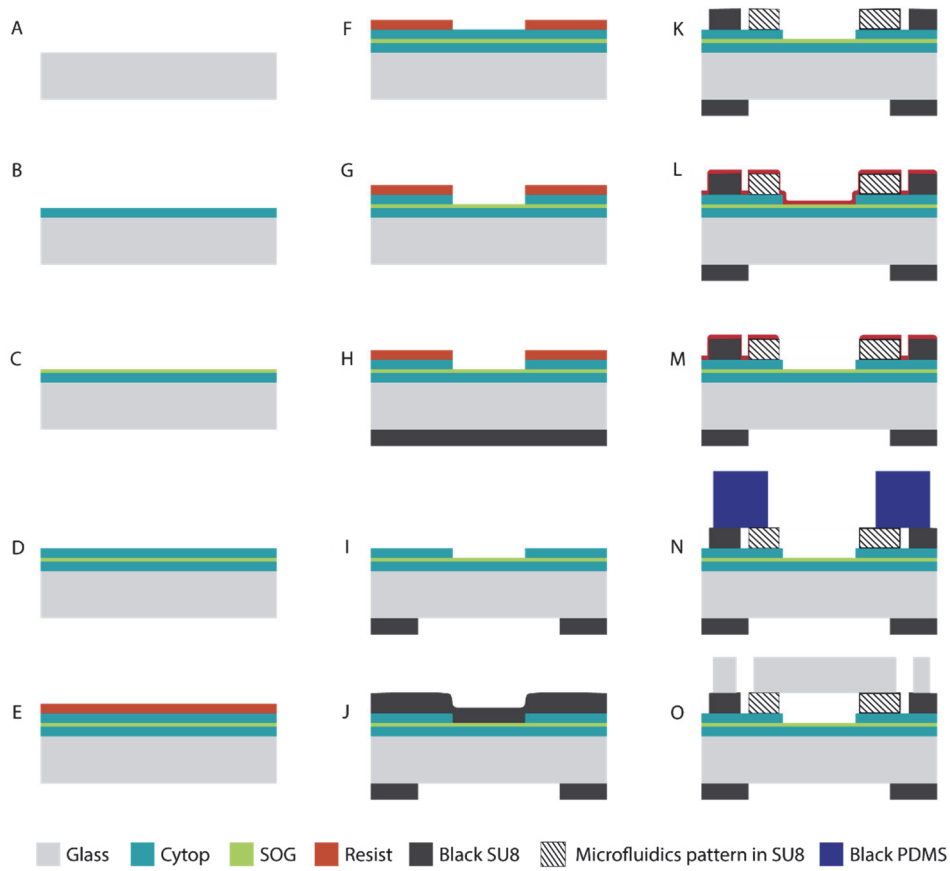

Figure 2.Typical processing flow of a waveguide device on glass with microfluidics ready for bilayer formation. A).Substrate preparation for Cytop coating. B) Cytop processing and activation. C) Spin on glass coating and activation. D) Cytop processing and activation E) Coating and exposure of the resist with the microfluidic patterns. F) Developing the resist. G) Reactive ion etching of the cladding to pattering the microfluidics in Cytop. H) Photolithography of black SU8 on the back side of the substrate with windows for microscopy. I) Developing the black SU8 layer. It will result in removing the photoresist on top of the substrate as well. J) Photolithography of black SU8 on top of the waveguide with Microfluidic pattern slightly bigger than the ones in Cytop. K) Developing the SU8 layer. L) Coating the waveguide with a protective layer and dicing. M) Patterning a fresh protective layer to protect the SU8, followed by oxygen plasma activation of the measurement area. N) The protective layer is removed. In case of well configuration a punched slab of black PDMS is placed on top of the measurement area. O) The protective layer is removed. If microfluidics needed, a glass substrate with hole for inlet and outlet are thermally bonded to the SU8 layer.

3.1 Substrate preparation

The common role of substrates is to act as solid support and provide stability to the device that is fabricated on top of it. Depending on the device and its application other properties of the substrate can be important, like its electrical properties, roughness, surface tension, adhesion, etc. Here the main criteria relates to good adhesion of the materials used during fabrication and high surface flatness, but the optical properties of the substrate, such as the amount of auto-fluorescence generated, may also be important. The choice of opaque or transparent substrates determines how the waveguide can be used in combination with different microscope setups. A transparent substrate makes the device compatible with inverted microscopes by allowing the detected light to be acquired through the substrate. This, in turn, enables for high numerical, oil-immersion objectives to be applied, thereby increasing the sensitivity and image resolution that can be obtained. Since most microscope objectives are corrected for glass substrates, and considering the low roughness, availability and low cost of commercially available substrates, glass was the obvious choice of substrate material. Nevertheless, the fragile nature of the 170 μm glass substrate needed to offer compatibility with oil immersion high NA objectives makes handling and dicing of the substrate extremely challenging.

3.2 Lower claddings

For the fabrication an A-type Cytop™, CTX-809A (Asahi Glass Co.) was used. Cytop, which is a fluorine based polymer is very hydrophobic, and the fluorine chains result in very low adhesion to contacting substrates. γ-Aminopropyl-triethoxy silane[a] (APTES) can be used as an adhesion promoter when using glass substrates according to the manufacturer. The functionalization was done by spin coating a freshly prepared 0.2%v solution of APTES in 95% ethanol prepared from 99.8% ethanol (Figure 2A). This was followed by a few minutes of baking to remove residual water and ethanol from the surface and also promote the binding of silane to the surface[40]. Cytop was spin coated on the silanized substrate at 900 rpm to achieve a 4um thick layer (Figure 2B). The curing of Cytop was done in a temperature controlled furnace under nitrogen with a glass beaker on top to reduce the solvent evaporation rate during baking and to improve surface flatness[41]. The temperature was ramped at 2.2°C/min from

[a] $H_2NC_3H_6Si(OC_2H_5)_3$

50°C to 80°C and held constant for one hour. A second ramp from 80°C to 250°C was followed with the same ramping rate and incubation time of 3 hours. The substrate was left to naturally cool down over night.

3.3 Core layer

A similar challenge to that of adhering Cytop to the substrate exists when it comes to the deposition of the core layer; poor adhesion to Cytop. For the core layer, the standard procedure to overcome this challenge was to electrically polarize the surface. For that a 20-30nm thin layer of Aluminum was deposited on the Cytop surface. After Aluminum deposition, Cytop monomers on the surface is believed to be oriented and their hydrophilic COOH end group faces the surface[41–43]. The Aluminum was removed using a NaOH based developer, maD331, prior to core layer deposition.

Silicon oxide was chosen as the material for the core layer of the waveguide because of its compatibility with many biological assays and protocols. Since Cytop has a low glass transition temperature of 108°C, one needs to devise a deposition technique that is compatible with fairly low temperature. Spin on glass (SOG) is a class of products that can provide us with that possibility. Although most SOG products require temperatures above 400 C for baking stage during curing, a longer baking time at lower temperature turned out be adequate in our case (Figure 2C). Here the baking was done in a vacuum oven at 120 C for 24 hours and cooled down for another 6-10 hours under vacuum.

3.4 Upper cladding

The procedure for the second cladding layer is very similar to that of the lower layer. To promote the Cytop adhesion, the core SOG layer was functionalized in the same way as the glass substrate. The Cytop layer was subsequently spun on the core layer with similar parameters as used for the lower layer. The baking was done in a vacuum oven, starting with 30 minutes incubation at 50°C followed by 30 min incubation at 80°C and 1 hour at 100°C. The temperature ramping between the steps was kept close to 1.6°C /min (Figure 2D).

3.5 Opening of the measurement area

To make measurements in an aqueous sample possible, it must come in contact with the evanescent field that propagates at the interface of the core layer. The opening in the upper cladding was made by reactive ion etching (RIE) (Figure 2G) through a photoresist pattern (Figure 2F), which defines the shape of the measurement area. The adhesion of the photoresist to the Cytop could be promoted in two ways; Aluminum deposition, or APTES treatment. The former procedure was explained above. The latter method was carried out by mild oxygen plasma treatment of the Cytop using a showerhead plasma chamber operated at 25W for 30 seconds. Afterwards, the sample was immediately immersed in a 2% aqueous APTES solution and kept for 10-20 minutes. This procedure improved the subsequent adsorption of APTES to Cytop and results in a rather good adhesion to the photoresist. Two positive photoresist (Figure 2E), AZ4532 (Microchemicals GmbH) and ma-P1225 (micro resist technology GmbH), along with their corresponding developers, AZ351B (Microchemicals GmbH) (1:4 water ratio) and ma-D 331 (micro resist technology GmbH) respectively, have been used for pattering the surface. To prevent defect formation in the waveguide, all necessary baking of the photoresist were done at 90 C. The etching was performed in an ICP/RIE tool (Oxford Plasmalab System 100) at RF and ICP[b] powers of 50W and 40sccm oxygen flow rate. The etching was monitored live with a laser interferometer. The etching continued for one minute after a plateau in the interferometry signal was observed, indicating the end of etching process.

3.6 Back layer

When coupling light into the waveguide structure by placing an optical fiber next to the waveguide facet, some of the light that is supposed to be coupled in the waveguide core, may leak into the supporting glass substrate. To obviate this adverse effect a thin light-absorbing layer was patterned on the back side of the substrate. For that purpose GMC1060 (Gersteltec), that is a SU-8 resist with black die, was mixed with SU-8 3005 and SU-8 3035 (MicroChem Corp.) in proper portions to get similar viscosity to that of GMC1060. The mixture was spin coated to a thickness of 30 μm on the back side of the glass substrate (Figure 2H). The layer went through soft baking at 65 ^{o}C and 90 ^{o}C for 10 and 25 minutes,

[b] Inductively Coupled Plasma

respectively, and exposed for 15 minutes to pattern an opening for objective to see through. The post bake parameters were set similar to that of the soft bake step. The layer was developed in mr-Dev600 (micro resist technology GmbH) for about 4 minutes (Figure 2I). During the development step the positive photoresist on the waveguide-side of the wafer will be also removed, making it ready for the next step.

3.7 Microfluidics

A benefit of being able to use an inverted microscope is that it makes easier access for possible microfluidics, which in turn makes experiments under controlled liquid flow possible. Moreover, it can improve handling and general stability of the experiment during the liquid exchange. In a closed system like a microchannel, evaporation is not an issue during long experiments and the risk of contamination from the environment will be reduced as well. However, the added-values of microfluidics come at the cost of more processing steps!

Microfluidics in SU8 has been chosen as the processing approach to make controlled micro-channels on the waveguide. In order to reduce the stray light, i.e. to shield the measurement window from environmental disturbances and loosely guided light in the usually transparent microfluidic layer, an SU8 containing a black die, GMC1060 (Gersteltec, Switzerland), was used. The product builds up a very high stress and has very bad adhesion to substrate. Moreover, the black die absorbs light even in UV range which result in decaying exposure dose through the film thickness while defining the channels by photolithography. To mitigate some of these problems, a customized mixture of GMC 1060 and SU8 3035 (MicroChem) was prepared and used. The mixture proved to have a lower stress in the film and better adhesion and bonding properties in practice.

Since the new mixture combines properties of both products, strictly following the processing guidelines of either of the product may not be a good choice. After finding the optimal conditions, the customized mixture was spun at 2000 rpm with acceleration and deceleration of 100 rpm/sec for 40sec (Figure 2J). APTES functionalization left on the Cytop from the previous step (see above) promotes a uniform and well adhered film. In order to achieve a better uniformity in the film, the resist was allowed to relax for 10 minutes after spinning. Soft baking was carried out at 65 C° and 90 C for 10 and 25 minutes respectively with a ramping rate of 2 C/min. The wafers were then allowed to

cool down to room temperature for the next 30 minutes (Figure 2J). The position of the microfluidic channels defined by a mask prior to exposure of the photoresist were aligned with the measurement windows previously etched in the Cytop and exposed in 15 consecutive steps of 1-minute exposure with 10 seconds of resting in between.

The post exposure step was performed similar to the soft baking step. The channels were developed and rinsed with a solvent based developer, mr-Dev 600 (Microchem), for 4 minutes followed by 1-minute soaking and rinsing in IPA (isopropyl alcohol), water and finally spin drying (Figure 2K).

3.8 Dicing

The dicing of the wafer does not only serve to separate the waveguide into individual chips. It also defines the quality of the extremely important facet and thus the efficiency of the in-coupling of light into the waveguides. The quality of the facet is thus one of the crucial parameters in waveguide fabrication; a good facet ensures a good and efficient coupling of light in the waveguide while a facet with smeared or detached layers with lots of debris and cracks resulting from bad dicing causes little or no possibility of light in-coupling. Several parameters can affect the dicing quality including the substrate material, adhesion of waveguide layers to each other and the waveguide to the underlying substrate, blade type and properties like grit size, concentration, and matrix material, feed rate and spindle speed, etc.

Two blade series from Disco, R07 and P1A851, with synthetic diamonds and grit size of 800 were tested. The blades were dressed at spindle speed of 30Krpm by making 10 cuts at 10mm/sec followed by another 10 cuts at 20mm/sec in GC3000PB50 dressing board. Photoresist on glass has been used as a model system to evaluate the effect of different dicing parameters on the chipping of the waveguide. A spindle speed of 30Krpm with a 0.5mm/sec feed rate was concluded to minimize the cracks and chipping for both blades.

To protect the measurement area of the waveguide and the SU8 layer from contamination, a photoresist layer was spun on the wafer (Figure 2L). Further investigation of dicing quality showed that the thicker the resist layer, the less chipping occurs on the waveguide facet. Due to the curvature of the blade and the 180-200 µm thick substrate, the depth of dicing affects how close the fiber can get to the chip's facet, which in turn affects the coupling efficiency and the

amount of stray light generated. On the other hand, if the substrate is diced through, because of rather poor adhesion of glass to the dicing tape, one risks damaging the blade. Here around 50 µm of substrate was left after dicing as a compromise between the two effects. The photoresist was removed with proper resist developer or remover after dicing.

3.9 Activating the measurement window

Even though the surface of the spin on glass core layer in the measurement window is flat (root mean squared surface roughness < 1 nm as measured with atomic force microscopy) and homogenous, its properties with regards to surface functionalization and compatibility with biological entities might have been compromised in the processing steps. Spontaneous formation of supported lipid bilayers is known to be critically dependent on the quality of the silicon oxide layer. Successfull formation of an SLB can thus be considerred as a sign that the surface properties of the core layer has been preserved. Oxygen plasma cleaning is commonly applied as treatment prior to forming supported lipid bilayers on glass and silicon oxide layers. Having spin on glass, which mainly consist of silica, oxygen plasma treatment turns out to be a reproducible method for surface activation. An oxygen plasma treatment would thus be feasible as a last step before carrying out an experiment using the waveguide. However, since now being enclosed in microfluidic channels, a different protocol must be adapted.

To find an alternative activation procedure that could be applied within a closed channel, several chemical cleaning procedures such as SDS, Hellmanex alternation, cleaning with 2M sulfuric acid, treatment with 7x[44] (P Biomedicals), and Liquinox[45] (Alconox) were tested. However, none of them showed any sign of a substrate resulting in reproducible and spontaneous bilayer formation. To circumvent this problem, the activation and cleaning was instead done before enclosing the microfluidic channels with glass-SU8 bonding. Since SU8 bonding performance degrades drastically upon exposure to oxygen plasma, another photolithography step, using AZ4532 or ma-P1225, was performed to protect the SU8 while exposing the measurement area (Figure 2M). The oxygen plasma cleaning was performed in a Harrick plasma chamber, PDC-002, at 30W for 40 minutes. The resist was then removed with a proper resist developer or mr-Dev 600 solvent based developer. No significant difference was observed between the resists and developers used during the process when it comes to bilayer

formation, although mr-Dev 600 might be preferred as it also removes the possible SU8 leftovers. Supported lipid bilayers could still be formed spontaneously on the waveguides weeks after the oxygen plasma treatment and bonding!

3.10 Bonding

The last processing step that has to be carried out in a cleanroom environment is bonding to seal the patterned channels on the chip. In this process a piece of glass with drilled holes for inlet and outlet was pressed on the SU8 layer at an elevated temperature. The quality and reproducibility of bonding depends on the pressure, temperature, the quality of SU8, surface cleanness, and the method of pressure application. Proper care was taken to make sure that SU8 bonding performance is not degraded during the fabrication process by using low temperature bakings and proper protection. Two different tools have been compared for bonding; SB6e (SUSS Microtech) and CNI v1 (NILT). SB6e is a substrate bonding tool is mainly designed for 6 inch wafers and has two metallic plates with rather high thermal capacitance where the sample is pressed in between, while CNI, mainly developed for nanoimprinting process, is equipped with a balloon which is filled with pressurized nitrogen that pushes the sample toward its ceramic chuck. The bonding procedure for both machines started with ramping the temperature to 70 C over 5 minutes. Thereafter, the pressure was gradually increased for the next 3 minutes up to 6 bar. After a few minutes of holding time, the temperature was raised to 90 C with a 2 C/min ramp rate and held there for 30 minutes to 2 hours depending on need. The chip was unloaded when the tool was cooled down to 50 C (Figure 2O). Although the CNI tool is limited to 10 bar pressure and requires the top substrate to be within the lower substrate, it reproducibly resulted in better bonding quality and performance relative to SB6e tool using similar bonding parameters. In case when the glass lid had a free hanging edge around the waveguide chip, it had to be placed on a proper holder that filled the gap under the free hanging glass to prevent it from cracking under pressure.

4 Image processing

The fabricated waveguide device, whether it is made on silicon or glass or equipped with microfluidics or without, provides a convenient way to confine the light illumination to the surface and renders low background in microscopy images. To evaluate the results of experiments, whether it is performed using an upright or an inverted microscope, or in fluorescence or scattering mode, one needs to go through the acquired images, and carefully monitor changes in each frame and/or step of the experiment. The information one searches for can be hidden in the appearance or disappearance of entities on the surface, changes in the intensity of the signal or correlations of signals measured in different microscopy channels, etc. To extract as much information from the microscopy images as possible, an image processing algorithm was developed in a MATLAB environment. In this chapter, it is described how the image processing algorithm works, including a presentation of how the main features embedded in the code are adopted to different kinds of experiments and experimental needs. To aid the understanding of the section, the different terms used are summarized in Table 1.

Table 1. Basic definitions in the image processing code

Image stack	A bundle of images saved into one file. Each image in the stack can be referred to with its frame number.
Background frame	An image usually taken prior to the experiment showing the initial condition of the surface. It is used as a point of comparison to discern what particles have been on the surface and what particles are new.
Experimental step	A state in the experiment when steady state has been reached and no changes in the number of immobilized objects are expected, but where changes in the properties (fluorescence or scattering) of the particles can still occur.
Channel	Refers to either fluorescence (WGF) or scattering (WGS) mode
Frame set	Defines which frames that belong to WGS or WGF in a given experimental step.
Reference frame	Representative image of a frame set, with respect to which newly added particles are detected relative to the previous experimental step. Information regarding particle location and the area associated with each particle is used, as a reference, for all frames within the corresponding frame set.

4.1 Preparation

The input file consists of ***image stacks*** obtained from the microscope camera. To start, the images need to be carefully aligned. This way one improves the chance that objects found in the same spots in consecutive frames are indeed the same object. Here, a basic image alignment was carried out by a Template Matching plugin[46] in ImageJ, but a similar function could have been implemented directly into the image-processing algorithm in MATLAB if needed.

Next, the user continues by defining the ***experimental steps*** of the experiment. An experimental step is part of the experiment during which no more objects are added to the surface. Therefore the algorithm does not need to look for new objects within the frames acquired in that phase. As an example, all frames acquired after saturated immobilization of irreversibly bound entities fall within the same experimental step, while if one needs to study the rate of adsorption of immobilized entities each frame represents a new step. Each experimental step can have two attributes, scattering and fluorescence, representing the two possible microscopy modes in the experiment. These attributes are also referred to as ***channels*** as they represent the microscopy channels in the experiment. A

frame set defines each of these attributes for an experimental step, by providing the indexes of the corresponding frames in the image stack. For each frame set a representative frame, called ***reference frame***, is selected. The regions recognized as particles in the reference frames are used to estimate variations in the properties of the particles in the frames within their corresponding frame sets. Moreover the user can provide ***background frames***, which show the initial conditions of the surface before the start of the experiment. The objects detected in the background frames will be excluded from the subsequent frames.

4.2 Image processing algorithm

The image processing starts with identifying the parts of the image in which data might have been deleted and pixels that contain no information after alignment of the frames. If a particle in one frame is superimposed on a deleted data on another frame, the code toggles a flag for that particle.

A few global criteria and one experimental-step-specific threshold need to be satisfied for an object in the image to qualify as a "valid" particle. Initially a background is estimated that will be used as a point of reference for the first intensity threshold. As most pixels of each frame correspond to background, the median intensity of a reference image provides an estimation of background for that frame. An intensity threshold coefficient, which is defined relative to the estimated background, is provided by the user. Any part of the image that passes that threshold will be included in a subsequent search for valid particles. Since sometimes the background is not uniform over the whole frame, the intensities of newly found areas are compared to their surrounding pixels. This provides a local point of comparison and ensures a faint particle lying over a relatively dim background not to be left undetected.

After each intensity threshold comparison, if an isolated region consists of a user-defined minimum number of connected pixels, it will be considered as a "valid" object, if not it is discarded.

Occasionally, especially in scattering mode, fringes appear between very bright neighbors that are located closely together. To avoid detection of these fringes as unique particles, every identified region is expanded a few pixels to let these parts connect to the parent particles. Since fringes have lower intensity than their "parents", comparing the pixels in the newly formed islands to a coefficient

of the average intensity of the islands, is used as an efficient exclusion principle of the fringes. This process usually does not disturb the parent particles and isolated particles with no fringes, although adjacent particles with drastically different intensities can be affected. In that case the faint particle will be excluded from the data set, as a compromise to avoid fringes being reported as a particle.

After applying a minimum pixel criteria, the remaining islands will be considered as the seed regions centered to the particles in the frame. Possible “holes” in the seed areas are then filled and single pixel protrusions are removed to have smooth boundaries around the particles. As a final touch all seed areas are expanded, without being connected, to ensure that the area engulfs the particle, and make the processing more robust against misalignment between the frames of an experimental step. This step does not affect the measured property of the particles. Nevertheless, one needs to take special care not to enlarge the assigned areas more than necessary, especially for cases with multiple experimental steps. Too large areas assigned to particles in one step will hinder the code finding the newly added particles in the following steps.

After processing all experimental steps, the code assigns a unique index to each particle and decides which particles are reliable for further analysis and which are not. The latter process starts with providing background frames, if available. The particles found in the background images are excluded from the processing if found also in the experimental steps. If particles that are independently found in the different channels (WGF and WGS) of the same step, are positioned on top of each other, they will be considered as one particle and share the same index. Particles that are not overlapping will receive unique individual indexes. If two regions in one channel share pixels with a region in another channel in a way that hinders finding other particles, all affected particles in both channels will be flagged as unreliable for that experimental step. If a particle in one channel overlaps with forbidden areas in the background of the other channel, although being reported, it will be flagged as a particle which was not checked in the latter channel. Forbidden areas include the deleted areas, pixels containing no information, and the areas assigned to particles of a previous step in that channel including background frames. If an identified particle touches the boundary of the image it also raises a flag, since it means that the particle may not be completely in the field of view.

When all particles have received their universal indexes, the code continues with assigning the background pixels to each particle. The background for a particle consist of a preset minimum number of pixels in the closest vicinity of the particle that are i) not part of any other particle in that channel of the current step, ii) the pervious steps or iii) the forbidden areas, including the particles found in the background frame. If for any reason the code encounters a problem finding the background area for a particle, it will be flagged as “problematic”.

After processing all particles, the code returns information for each particle, such as the intensity of the particle, background value, and area. All flagged information is passed on to the user together with quantitative information, aiding the decision by the user regarding which particles that are reliable enough for the intended analysis. An example of how image processing has resulted in finding new particles landing on the surface is provided in Figure 3.

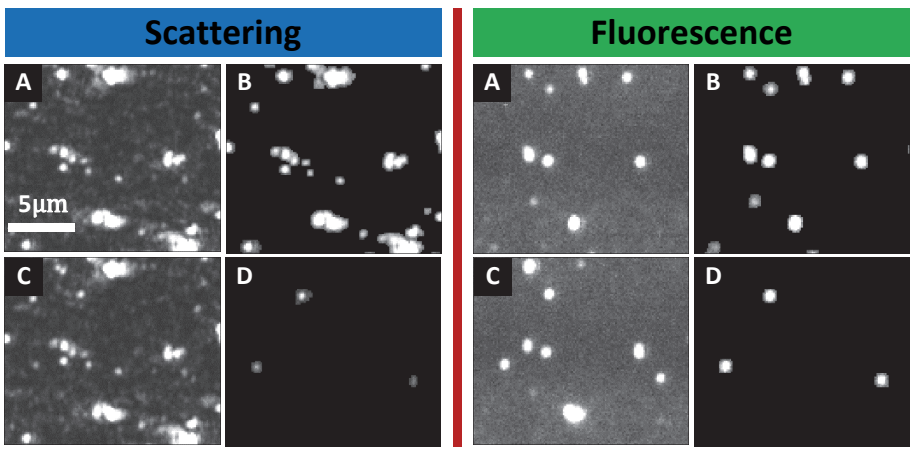

Figure 3. Finding new vesicles in consecutive frames in fluorescent and scattering channels. A) Initial frame. B) Regions detected by the image processing that include vesicles in the initial frame. C) Same area after absorbing more vesicles. D) Newly absorbed vesicles detected by the image processing.

5 Summary of results

The devices fabricated on silicon and glass has been put in use. Several experiments have been conducted both to benchmark the waveguide imaging and to explore its adaptability to biological experiments. The image processing code described earlier was used to process the experimental data and assess the performance of the device in waveguide scattering, waveguide fluorescent and Epi modes. These efforts are presented and discussed in detail in the appended papers. The following sections provide a brief prologue to the work detailed in these papers.

5.1 Summary of appended paper I

The first paper in this series is mainly focused on the fabrication and characterization of the waveguide platform developed to be compatible with upright microscopes, i.e. being based on an opaque silicon substrate. A high quality waveguide illumination device with low background requires a cladding with a refractive index close to water. Fluorinated polymers are one of the very few martials which satisfy that criteria but in turn they impose serious challenges in the fabrication process. The paper introduces a low temperature fabrication scheme that overcomes those challenges. We were able to fabricate

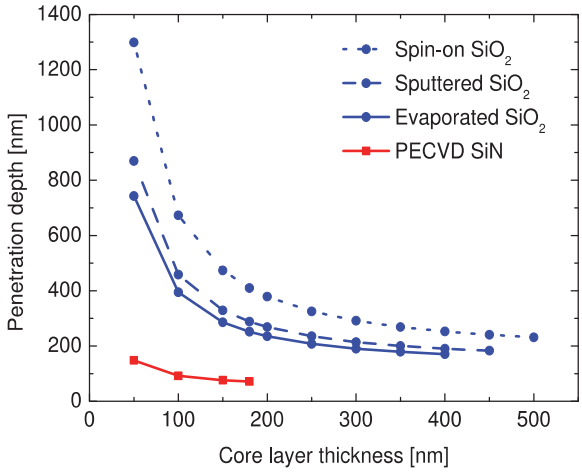

Figure 4. Calculated penetration depth of optical waveguides with Cytop cladding, for different core layers at 532nm TE excitation.

a working waveguide platform with four different core materials (Spin on SiO_2, sputtered SiO_2, evaporated SiO_2 and SiN). Based on the dispersion relation of these material the penetration depth was simulated at 532nm (Figure 4) which shows a wide tenability window for the penetration depth, ranging from below 100 nm to above 1 μm.

Microscopy images of fluorescent latex beads have been used to assess the performance of waveguides with SOG core layer in scattering and fluorescent modes relative to fluorescent Epi microscopy. The signal to noise (SNR) and signal to background (SBR) were calculated in the presence of different bead concentration in the bulk solution for each mode. The results, depicted, Figure

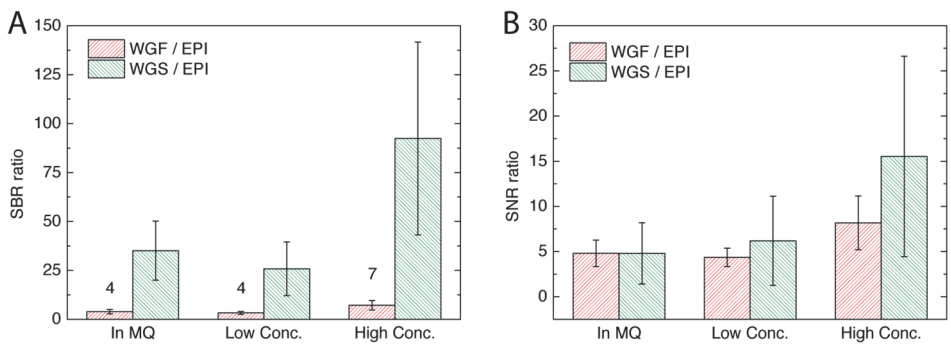

Figure 5. Assessment of (A) signal to noise (SNR) and signal to background (SBR) of waveguide fluorescent (WGF) and scattering (WGS) modes relative to epi fluorescent microscopy for images of 100nm fluorescent latex beads on the waveguide surface at different concentration of beads in the solution.

5 show superior performance for waveguide modes relative to epi especially in scattering.

5.2 Summary of appended paper II

The waveguide platform on silicon that was fabricated and characterized in paper I has been used to demonstrate its applicability and sensitivity in various biological essays. Detection of individual lipid vesicles and the interaction of certain biomolecules with them has been studied simultaneously in fluorescent and scattering mode. As a foundation for these experiments, the performance of the waveguide microscopy setup was evaluated using 150 nm rhodamine labeled vesicles. The intensity of scattering versus fluorescent signals for over 2000 vesicles is presented in Figure 6A. The histogram of the scattering and fluorescent intensities are also depicted in hatched green and red bars on Y an X axes, respectively. The solid red bars show the sub population of vesicles only found in fluorescent but not scattering mode, thus defining the detection limit

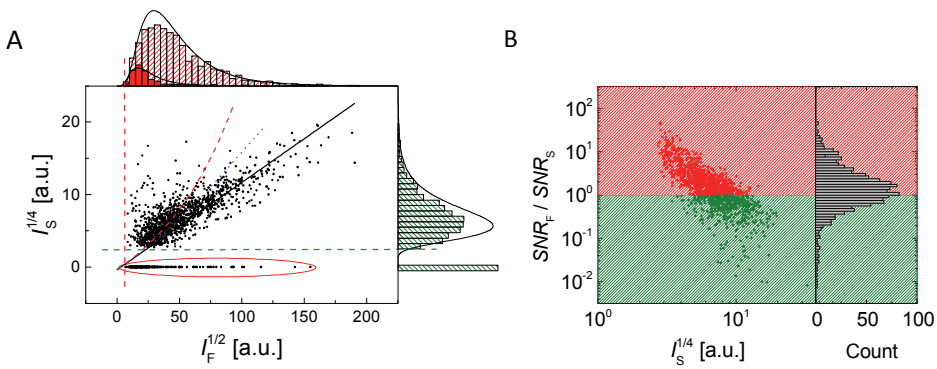

Figure 6. Scattering and fluorescence intensities from individual vesicles, (A) scaling with the powers 1/4 and 1/2 respectively for 2000 single fluorescently labeled vesicles with average diameter of 150 nm. The plot is expected to be linear provided IS∝r4 and IF∝r2. The distributions of the scattering (green) and fluorescence (red) intensities have been projected onto the y and x axis, respectively, and correspond to the size distribution of the vesicles. The red vertical and green horizontal dashed lines indicate the limit of detection. The black straight line, red dashed curve, and blue dotted curve show the theoretically predicted behavior with 3 different assumptions. B) SNRF/SNRS for all measured vesicles as function of scattering intensity. Ratio SNR_F/SNR_S for all measured vesicles as a function of scattering intensity, with the SNR defined as $I_{S/F}/\sigma_{S/F}$, where $\sigma_{S/F}$ is the standard deviation of the background noise. The histogram to the right shows the distribution of this ratio indicating that on average the fluorescence signal gives a better SNR than the scattering signal for these particular vesicles (containing 1 wt % rhodamine-PE lipids) in this size range.

for the scattering mode. Compared to NTA data, 80 nm is concluded as the detection limit of the lipid vesicles in waveguide scattering.

Furthermore, the signal to noise ratio (SNR) in scattering and fluorescence modes was compared for vesicles. In Figure 6B, the ratio of the SNR in fluorescence and scattering is plotted versus the forth root of the scattering signal, which corresponds to the radius of the vesicles. As expected, the scattering signal result in much better signal to noise for large vesicles, as the scattering cross section increases with for 4^{th} power of radius, in comparison to 2^{nd} power in fluorescence mode, due to labeling of the membrane shell only.

5.3 Summary of appended paper III

Paper III is an expansion of paper I which turned out to be highly demanding. Here the fabrication process presented in paper I was adapted and optimized for glass substrates. This not only allows the waveguide platform to be used on inverted microscopes in combination with high NA objectives but also gives the user access to the top of the platform, allowing for microfluidic channels to be incorporated directly on the waveguide, thus expanding the applicability and liquid handling of the device.

To evaluate the impact of the numerical aperture on the quality of the waveguide microscopy, fluorescent and scattering images of 100nm fluorescent latex beads were captured at different numerical apertures (Figure 7A). Using the previously described image processing algorithm we were able to evaluate how the background, intensity (signal) and signal to background (SBR) evolves with NA for over 1000 particles. For each microscopy mode these parameters were normalized for each particle to their value at NA 0.5. The averaged value is depicted in Figure 7B, which shows and increasing trend for the signal-to-background ratio, which is the most important parameter for particle detection, up to NA = 1.1. For larger NA, the SBR decrease as some optical anomalies appear in the acquired image, especially in scattering mode (Figure 7A).

To test the detection limit of the waveguide scattering, it was used to detect SV40 virus adsorbed on GM1-containing POPC bilayer. This failed, however, probably because the strong reduction in intensity versus particle radius. To verify SV40 binding, the virus was instead identified with a 100nm rhodamine labeled POPC vesicles with 5% GM1 content. The images where acquired in both fluorescence and scattering modes and processed for new objects landing in the

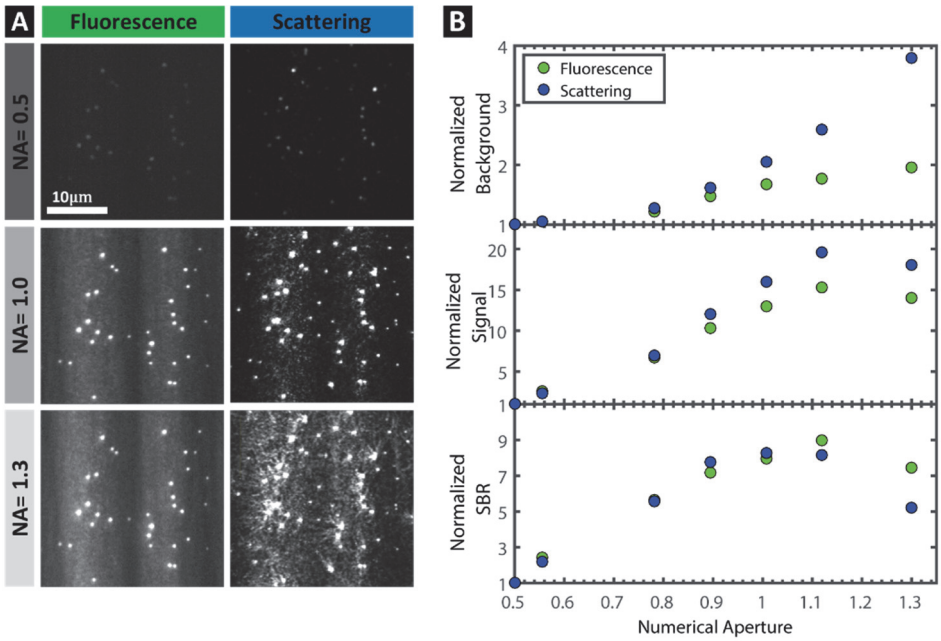

Figure 7. A) 100nm Fluorescent Latex beads on the waveguide excited 488nm laser at 7mW captured at different numerical aperture values in scattering and fluorescent modes with 0.5 sec and 4 sec exposure respectively. B) Assessment of waveguide performance in scattering and fluorescence modes with numerical aperture by averaging the corresponding property of over 1000 fluorescent latex beads. All properties in fluorescence and scattering are normalized to their initial values at NA 0.5.

measurement area during the tagging step. The fluorescent image maps out the virus position and if the same spot is independently detected in both fluorescent and scattering modes, we report a successful detection. This way two third of all viruses found in the fluorescent image could be detected in scattering as well. Figure 8 shows the histogram of the fluorescent signal for all vesicles detected in fluorescence mode (all bars) overlaid with the histogram of those that were also detected in scattering (hatched blue and green). The one third of vesicles that were not detected in scattering all occupy the lower end of the fluorescent intensity distribution. Although some of the implied limitation still originates from image analysis, it is to be expected that the detection of smaller vesicles is easier in fluorescent than scattering (as discussed in the section of Paper II). From this analysis we were also able to define the present detection limit to correspond to lipid vesicle with a diameter of 100 nm, which is comparable to the waveguide fabricated on a silicon substrate. .

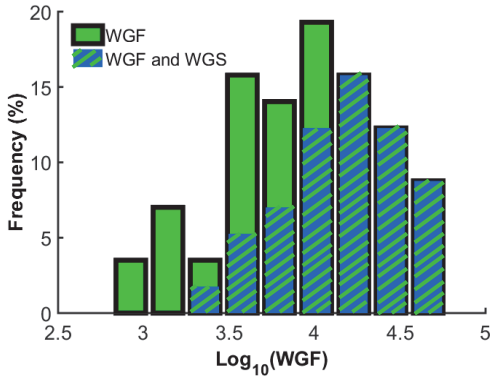

Figure 8. Green bars represent fluorescence intensity distribution of vesicles attached to SV40 viruses on the bilayer. The hatched blue:green bars represent those fluorescent vesicles that are also found in the corresponding scattering frame.

6 Outlook

So far we have managed to fabricate and demonstrate a working waveguide on glass substrates that is equipped with microfluidics channels, but we are yet to explore the opportunities that the microfluidics provide. Considering the strength and expertise in the group, an experiment can be designed to evaluate the size distribution of biological entities by sheering them on a bilayer and assessing their size from their diffusion coefficient measured by single particle tracking analysis. This will require even more efficient background correction algorithms and incorporation of particle positioning and tracking algorithms, but will make it possible to correlate scattering intensity with particle size, which is not easy with alternative methods, such as nanoparticle tracking analysis.

On the device level, simulations in paper I show how the penetration depth can be adjusted with the choice of the core material and its thickness. By reducing the core thickness and using a material with lower refractive index, the penetration depth can be increase above 1µm, which wil allow for illumination of the whole volume of a shallow microfluidic channel made in the cladding of the waveguide. In theory such a device can be used to detect and characterize close to 100% of entities inserted in the channel in both scattering and fluorescence. The evanescent field would also penetrate much deeper into cells than being possible with conventional TRIF.

Another interesting modification of the waveguide platform that can be explored is the use of a transparent conductive layer like ITO as waveguide core layer, or to deposit thin ITO coatings on the core of layer of the waveguide. If implemented successfully, it will allow probing or inducing electrochemical activities on the surface/in the solution in combination with waveguide scattering or fluorescent imaging, which adds another dimension to the acquired data.

The configuration of the waveguide allows for local surface plasmon resonance (LSPR) excitation as well. We have already evaluated the possibility of incorporating gold plasmonic disk on the waveguide, as a foundation for further work. Not only can the plasmonic structures be used for sensing schemes, but they can also be used as a calibration reference for the illumination intensity between the experiments, which will be a central component for quantitative scattering-based imaging.

Acknowledgments

I would like to express my gratitude to *Fredrik Höök* for all the help and supervision he invested in me in these years. Without his support in critical moments you have not been reading “this”!

I would like to thank *Björn Agnarsson* not only for the supervision during the work and being patient but more importantly for being available at the moment of need.

I would also like to thank *Mikael Käll* and consequently *Srdjan Acimovic* and *Ruggero Verre* for being generous with lending precious optical components to people in need!

I definitely need to take this opportunity to thank *Julie gold* for her guidance and help along the road that has brought me so far to the licentiate.

I would also like to thank the following people:

Déborah Ruppert, for all the life advises!

Francesco Mazzota for all our time in cleanroom!

Nagma Parvin for spreading the virus!

Hossein Agheli, for the discussions that we used to have when you were around!

Silver Jõemetsa for proof reading your officemate’s work!

And all of the current and former members of *biological physics*, *chemical physics* and *bionanophotonics* for the coffee breaks, cakes, chats, lunches, celebrations, …

References

1. Brigger, I., Dubernet, C. & Couvreur, P. Nanoparticles in cancer therapy and diagnosis. *Adv. Drug Deliv. Rev.* **54,** 631–651 (2002).

2. Gao, X., Cui, Y., Levenson, R. M., Chung, L. W. K. & Nie, S. In vivo cancer targeting and imaging with semiconductor quantum dots. *Nat. Biotechnol.* **22,** 969–976 (2004).

3. Murray, L. J., Dincă, M. & Long, J. R. Hydrogen storage in metal–organic frameworks. *Chem. Soc. Rev.* **38,** 1294 (2009).

4. Whitesides, G. M. The origins and the future of microfluidics. *Nature* **442,** 368–73 (2006).

5. Mannsfeld, S. C. B. *et al.* Highly sensitive flexible pressure sensors with microstructured rubber dielectric layers. *Nat. Mater.* **9,** 859–64 (2010).

6. Lavrik, N. V., Sepaniak, M. J. & Datskos, P. G. Cantilever transducers as a platform for chemical and biological sensors. *Rev. Sci. Instrum.* **75,** 2229–2253 (2004).

7. Barsan, N., Koziej, D. & Weimar, U. Metal oxide-based gas sensor research: How to? *Sensors Actuators, B Chem.* **121,** 18–35 (2007).

8. Yazdi, N., Ayazi, F. & Najafi, K. Micromachined inertial sensors. *Proc. IEEE* **86,** 1640–1658 (1998).

9. Willets, K. A., Duyne, R. Van & Van Duyne, R. P. Localized Surface Plasmon Resonance Spectroscopy and Sensing. *Annu. Rev. Phys. Chem.* **58,** 267–297 (2007).

10. Meinardi, F. *et al.* Highly efficient large-area colourless luminescent solar concentrators using heavy-metal-free colloidal quantum dots. *Nat. Nanotechnol.* (2015). doi:10.1038/nnano.2015.178

11. Siahrostami, S. *et al.* Enabling direct H2O2 production through rational electrocatalyst design. *Nat. Mater.* **12,** 1137–43 (2013).

12. Anker, J. N. *et al.* Biosensing with plasmonic nanosensors. *Nat. Mater.* **7,** 442–453 (2008).

13. Jonsson, M. P., Dahlin, A. B., Feuz, L., Petronis, S. & Höök, F. Locally functionalized short-range ordered nanoplasmonic pores for bioanalytical sensing. *Anal. Chem.* **82,** 2087–94 (2010).

14. Liedberg, B., Nylander, C. & Lunstr??m, I. Surface plasmon resonance for gas detection and biosensing. *Sensors and Actuators* **4,** 299–304 (1983).

15. McDonald, J. C. *et al.* Fabrication of microfluidic systems in poly(dimethylsiloxane). *Electrophoresis* **21,** 27–40 (2000).

16. Kim, D. S., Lee, S. H., Ahn, C. H., Lee, J. Y. & Kwon, T. H. Disposable integrated microfluidic biochip for blood typing by plastic microinjection moulding. *Lab Chip* **6,** 794–802 (2006).

17. Srinivasan, V., Pamula, V. K. & Fair, R. B. An integrated digital microfluidic lab-on-a-chip for clinical diagnostics on human physiological fluids. *Lab Chip* **4,** 310–315 (2004).

18. Croft, W. J. *Under the Microscope: A Brief History of Microscopy*. (World Scientific, 2006).

19. Moerner, W. & Kador, L. Optical detection and spectroscopy of single molecules in a solid. *Phys. Rev. Lett.* **62,** 2535–2538 (1989).

20. Hell, S. W. & Wichman, J. Breaking the diffraction resolution limit by stimulated emission: stimulated-emission-depletion fluorescence microscopy. *Opt. Lett.* **19,** 780 – 782 (1994).

21. Betzig, E. *et al.* Imaging intracellular fluorescent proteins at nanometer resolution. *Science* **313,** 1642–1645 (2006).

22. Axelrod, D., Burghardt, T. P. & Thompson, N. L. Total Internal Reflection Fluorescence. *Annu. Rev. Biophys. Bioeng.* **13,** 247–268 (1984).

23. Tokunaga, M., Kitamura, K., Saito, K., Iwane, A. H. & Yanagida, T. Single molecule imaging of fluorophores and enzymatic reactions achieved by objective-type total internal reflection fluorescence microscopy. *Biochem. Biophys. Res. Commun.* **235,** 47–53 (1997).

24. Axelrod, D. Total internal reflection fluorescence microscopy in cell biology. *Traffic* **2,** 764–774 (2001).

25. Axelrod, D. Total internal reflection fluorescence microscopy. *Methods Cell Biol.* **30,** 245–70 (1989).

26. Prieve, D. C. & Frej, N. a. Total internal reflection microscopy: a

quantitative tool for the measurement of colloidal forces. *Langmuir* **6,** 396–403 (1990).

27. von Olshausen, P. & Rohrbach, A. Coherent total internal reflection dark-field microscopy: label-free imaging beyond the diffraction limit. *Opt. Lett.* **38,** 4066–9 (2013).

28. Bally, M. *et al.* Interaction of single viruslike particles with vesicles containing glycosphingolipids. *Phys. Rev. Lett.* **107,** 1–5 (2011).

29. Gunnarsson, A., Jönsson, P., Marie, R., Tegenfeldt, J. O. & Höök, F. Single-molecule detection and mismatch discrimination of unlabeled DNA targets. *Nano Lett.* **8,** 183–188 (2008).

30. Tabaei, S. R., Rabe, M., Zetterberg, H., Zhdanov, V. P. & Höök, F. Single lipid vesicle assay for characterizing single-enzyme kinetics of phospholipid hydrolysis in a complex biological fluid. *J. Am. Chem. Soc.* **135,** 14151–14158 (2013).

31. Agnarsson, B., Ingthorsson, S., Gudjonsson, T. & Leosson, K. Evanescent-wave fluorescence microscopy using symmetric planar waveguides. *Opt. Express* **17,** 5075 (2009).

32. Hill, D. J., Pinion, C. W., Christesen, J. D. & Cahoon, J. F. Waveguide Scattering Microscopy for Dark-Field Imaging and Spectroscopy of Photonic Nanostructures. *ACS Photonics* **1,** 725–731 (2014).

33. Hassanzadeh, A., Ma, H. K., Dixon, S. J. & Mittler, S. Visualization of the solubilization process of the plasma membrane of a living cell by waveguide evanescent field fluorescence microscopy. *J. Biomed. Opt.* **17,** 076025 (2012).

34. Grandin, H. M., Städler, B., Textor, M. & Vörös, J. Waveguide excitation fluorescence microscopy: A new tool for sensing and imaging the biointerface. *Biosens. Bioelectron.* **21,** 1476–1482 (2006).

35. Nahar, Q. *et al.* Waveguide evanescent field scattering microscopy: Bacterial biofilms and their sterilization response via UV irradiation. *J. Biophotonics* **7,** 542–551 (2014).

36. Agnarsson, B. *et al.* Evanescent Light-Scattering Microscopy for Label-Free Interfacial Imaging: From Single Sub-100 nm Vesicles to Live Cells. *ACS Nano* **9,** 11849–11862 (2015).

37. Zhang, H., Nie, S., Etson, C. M., Wang, R. M. & Walt, D. R. Oil-sealed femtoliter fiber-optic arrays for single molecule analysis. *Lab Chip* **12,**

2229 (2012).

38. Kogelnik, H. in 13–81 (1975). doi:10.1007/978-3-662-43208-2_2

39. Hunsperger, R. G. *Integrated Optics*. (Springer New York, 2009). doi:10.1007/b98730

40. Li, P., Lei, N., Sheadel, D. a., Xu, J. & Xue, W. Integration of nanosensors into a sealed microchannel in a hybrid lab-on-a-chip device. *Sensors Actuators, B Chem.* **166-167,** 870–877 (2012).

41. Agnarsson, B. *et al.* Fabrication of planar polymer waveguides for evanescent-wave sensing in aqueous environments. *Microelectron. Eng.* **87,** 56–61 (2010).

42. Degenaar, P. *et al.* A Method for Micrometer Resolution Patterning of Primary Culture. **376,** 367–376 (2001).

43. Grohens, Y., Schultz, J. & Prud'homme, R. E. PMMA conformational changes on g-alumina powder: influence of the polymer tacticity on the configuration of the adsorbed layer. *Int. J. Adhes. Adhes.* **17,** 163–167 (1997).

44. Pace, H. P., Sherrod, S. D., Monson, C. F., Russell, D. H. & Cremer, P. S. Coupling supported lipid bilayer electrophoresis with matrix-assisted laser desorption/ionization-mass spectrometry imaging. *Anal. Chem.* **85,** 6047–6052 (2013).

45. Pace, H. *et al.* Preserved Transmembrane Protein Mobility in Polymer-Supported Lipid Bilayers Derived from Cell Membranes. *Anal. Chem.* **87,** 9194–9203 (2015).

46. O'Dell, W. Template Matching. at <http://rsb.info.nih.gov/ij/plugins/template-matching.html>